Emptying of a bottle: How a robust pressure-driven oscillator coexists with complex two-phase flow dynamics

Samuel Mer, Olivier Praud, Jacques Magnaudet, Véronique Roig

Emptying of a bottle: How a robust pressure-driven oscillator coexists with complex two-phase flow dynamics

Samuel Mer*, Olivier Praud, Jacques Magnaudet, Veronique Roig

Institut de Mécanique des Fluides de Toulouse, IMFT, Université de Toulouse - CNRS, Toulouse, France

ARTICLE INFO

Keywords:
Bubbly flow
Multi-scale flow
Taylor bubble

ABSTRACT

The emptying of a bottle is one of the most common two-phase flows encountered in everyday's life fluid mechanics. We report on a detailed experimental analysis of this flow configuration covering a wide range of neck-to-bottle diameter ratios, d^*, and initial filling ratios, $\mathcal{F}$. The joint use of a pressure sensor at the top of the bottle and a shadowgraph technique to track the evolution of the upper liquid surface allows the average gas volume fraction in the fluid column to be computed throughout the discharge. Variations of the bottle emptying time, gas content, and characteristics of the pressure signal as a function of d^* and/or $\mathcal{F}$ are analyzed, and scaling or evolution laws are derived. A specific focus is put on the initial transient stages following the neck opening, especially on the nature and growth of the first bubble that reaches the upper free surface. Over a wide range of d^*, this bubble takes the form of a large spherical cap or Taylor bubble, the rise speed of which is controlled by the bottle diameter. Such a bubble directly emerges from the neck for large enough d^*, but rather results from successive coalescence of smaller bubbles for small d^*. Whatever d^*, the volume of this leading bubble increases over time, since a fraction of the small bubbles swarm trailed in its wake merges with its back face. This coalescence-induced growth is quantified through a simple model.

1. Introduction

Liquid-gas two-phase flows are ubiquitous in Nature and everyday's life fluid mechanics. Who has never been amazed by the formation of bubble trails in a glass of Champagne or by the frothy foam sitting on top of a beer? Some of the physical phenomena at stake in bubbly drinks were recently reviewed by Zenit and Rodríguez-Rodríguez (2018). However bubbles are not involved only in alcoholic drinks and one of the first bubbly two-phase flows encountered in a human life probably stands in the emptying of a water bottle. Despite its commonness and apparent simplicity, this flow exhibits rich physics and can be seen either as a complex nonlinear oscillator (Kohira et al., 2012) or a complex multi-scale gas-liquid flow (Mer et al., 2018), or even a liquid sandglass - as the liquid discharge remains almost constant during the whole process (Schmidt and Kubie, 1995). Indeed, all along the discharge, large air bubbles with diameters of the order of the bottle neck are periodically generated and rise within the bottle, until they burst at the free surface beneath its top. While ascending, these large bubbles undergo successive break-up sequences, yielding swarms of smaller bubbles, part of which may coalesce again and participate into the regeneration and reconfiguration of the large bubble population.

The first studies of this flow configuration reported in the literature assessed the influence of geometrical parameters such as the bottle shape and neck diameter (or shape) on the global emptying time (e.g. Whalley, 1987; Whalley, 1991; Schmidt and Kubie, 1995; Kordestani and Kubie, 1996; Tang and Kubie, 1997). These contributions showed that: (i) the liquid discharge rate remains constant during the whole emptying process whatever the initial filling ratio; (ii) the averaged pressure difference between the top air buffer and the ambient medium scales well with the hydrostatic head corresponding to the height of the water column; (iii) the emptying time is influenced by the bottle inclination angle, neck shape, and liquid temperature. Previous studies were extended by Héraud (2002), Clanet et al. (2004) and Clanet and Searby (2004), hereinafter referred to as CS, to cover a wide range of bottle shapes and dimensions. In particular, CS derived a general scaling law for the emptying time T_e of cylindrical bottles with length L and diameter D in the form

$$T_e \approx 3.0 \frac{L}{\sqrt{gD}} d^{*-5/2} \tag{1}$$

* Corresponding author.
E-mail addresses: samuel.mer@imft.fr (S. Mer), magnau@imft.fr (J. Magnaudet).

https://doi.org/10.1016/j.ijmultiphaseflow.2019.05.012

where $d^* = d/D$ is the normalized neck diameter and g denotes gravity. This scaling law emphasizes the fact that the geometrical ratio d^* plays an essential role in the emptying dynamics.

A second class of studies analyzed the emptying process as a non-linear oscillator, the liquid mass and top air buffer playing the role of a mass and a spring, respectively. These studies focused on small d^*, a condition under which the flow exhibits an on-off oscillatory behavior. Tehrani et al. (1992) proposed a model aimed at predicting the pressure fluctuation amplitude in the top air buffer in an idealized configuration. In their work, the bottle is reduced to a cubic tank, with a typical size of 25 cm, and the neck to a 60 cm long straw with a diameter up to 25 mm, i.e. $d^* < 0.1$. The straw-like neck geometry results in a large pressure loss at the bottle neck, which triggers the occurrence of on-off oscillations. Under these conditions, four stages were identified during one oscillation period: (i) liquid downflow; (ii) bubble formation and rise in the neck; (iii) bottle re-pressurization, and (iv) neck refill. Results provided by the model revealed good agreement with the experiments. Kohira et al. (2012) carried out an experimental and theoretical study of single and coupled on-off plastic bottle oscillators. They observed the emergence of in- and anti-phase synchronization, depending on the nature of the coupling. Jia et al. (2016) modeled these two distinct synchronization scenarios by considering time-dependent nonlinear terms resulting from the asymmetry between the liquid ejection and bubble admission processes. CS predicted the evolution of the oscillation period during the emptying process by integrating the Euler equation throughout the flow, assuming a schematic variation of the velocity distribution close and far from the neck. Their approach is not limited to the on-off oscillating behavior and can be applied to larger d^*. Its predictions reveal a fairly good agreement with experimental data over a broad range of d^*, suggesting that it captures the dominant mechanisms by which the neck diameter influences the oscillation period.

In a recent work, we highlighted how rich the bottle emptying process is from the point of view of multi-scale gas-liquid flow processes (Mer et al., 2018). In particular, we showed that this configuration provides a complete and difficult test case for validating multi-scale modeling approaches currently under development (Deendarlianto et al., 2011; Hansch et al., 2012; Montoya et al., 2015; Gada et al., 2017; Mimouni et al., 2017). The rigorous validation of such modeling approaches, and of the computational codes in which they are implemented, requires detailed and reliable experimental databases in which the gas phase within the water column is properly characterized. Local gas volume fraction measurements make use of optical probes (Suzanne et al., 1998; Raimundo et al., 2016), image processing (Lau et al., 2013) or LDA techniques (Kulkarni et al., 2001; Gandhi et al., 2008). However, given the highly intermittent nature of the flow in the present case, extracting relevant indicators from local gas fraction measurements with the goal of validating multi-scale models is not straightforward. Conversely, coupling a local pressure determination with an optical technique, such as shadowgraph, may give access to the average gas volume fraction in the water column. More precisely, assuming the pressure to be uniform within the air buffer at the top of the bottle, and equal to the atmospheric pressure outside the bottle, the coupling of a differential pressure sensor located within this buffer with an optical detection of the upper surface of the liquid column allows the space-averaged gas volume fraction to be determined.

The present paper reports on an experimental investigation of the emptying process in water 'bottles' with various neck diameters, based on the latter approach. By considering contrasting flow conditions, it aims at clarifying the role of the time-evolving two-phase flow that develops within the bottle on the emptying dynamics. Under some of these flow conditions, the fluid region is merely crossed by bubbles rising almost in line. Conversely, it rather looks as a dense and strongly agitated gas-liquid mixture under other conditions. Last, the flow configuration may evolve along the emptying process, from a quiescent liquid with large rising bubbles in the early stage, to a dense and strongly agitated bubbly flow when the liquid content has decreased significantly. The common thread of this investigation is to gain some insight into the influence of this complex two-phase flow on the oscillatory behavior of the overall system and *vice versa*.

The experimental facility along with the measurement technique are presented in Section 2. Section 3 reports qualitative observations of the flow structure and evolution, first describing the successive stages encountered during the emptying process within the top air buffer and the two-fluid column. Then, an overview of the two-phase flow structure and gas content is provided in Section 3.2. Global results are discussed in Section 4, starting with variations of the emptying time with the bottle geometry in Section 4.1, while some features of the pressure signal are analyzed in Section 4.2. The coupled measurement technique is used to determine the evolutions of the free surface and the gas content in the water column; these evolutions are discussed in Sections 4.3 and 4.4, respectively. Section 5 focuses on the early stages of the emptying process, with a special emphasis on the initial pressure transient (Section 5.1) and the characteristics of the first rising gas entity (Section 5.2). Section 6 summarizes the main findings of the study and draws some prospects, especially with respect to modeling issues.

2. Experimental set-up and measurement techniques

The device, measurement techniques and experimental protocol are similar to those employed by Mer et al. (2018). Their description is summarized below for the sake of self-consistency.

2.1. Experimental set-up

The experimental set-up (Fig. 1) consists of a Plexiglas^{TM} cylindrical vessel with diameter $D = 114$ mm and height $L = 800$ mm. The top end of the cylinder is closed with a blank flange, while its bottom section has a central circular thin-walled hole with a diameter d. The hole was manufactured with a beveled edge making a sharp 20° angle with the cylinder base. This bottom part is interchangeable and allows the neck diameter to be varied from 13 to 80 mm. The bottle neck is closed with a gate mounted on two hinges and equipped with five electromagnets ensuring a fast opening. Before a test, the gate is closed, the valves v_{in} and v_{out} are opened and the bottle is filled up to an altitude $z = z_0$ with tap water, using the circulation pump. Once filling is completed, the pump is turned off and the two valves are closed. As v_{out} remains opened during the filling process, the initial pressure at the top of the bottle is the atmospheric pressure, p_{atm}. The gate is quickly opened at time $t = 0$. Water starts to flow out of the bottle in a succession of jets separated by the generation of large air bubbles at the neck. Then, these bubbles rise within the water column and reach the free surface after a sequence of complex topological changes. In what follows, the tank normalized outlet diameter, d^*, and initial filling ratio, $\mathcal{F} = z_0/L$, are varied in the range $0.18 \leq d^* \leq 0.7$ and $0.24 \leq \mathcal{F} \leq 1$, respectively. The density and kinematic viscosity of the water used in the experiments, performed at room temperature, are $\rho_l = 997\,\mathrm{kg\,m^{-3}}$ and $\nu_l = 1 \times 10^{-6}\ \mathrm{m^2\,s^{-1}}$, respectively.

2.2. Measurement techniques

The air pressure at the center of the top end of the bottle, p_{top}, is monitored thanks to a pressure sensor (Keller, PR-23).

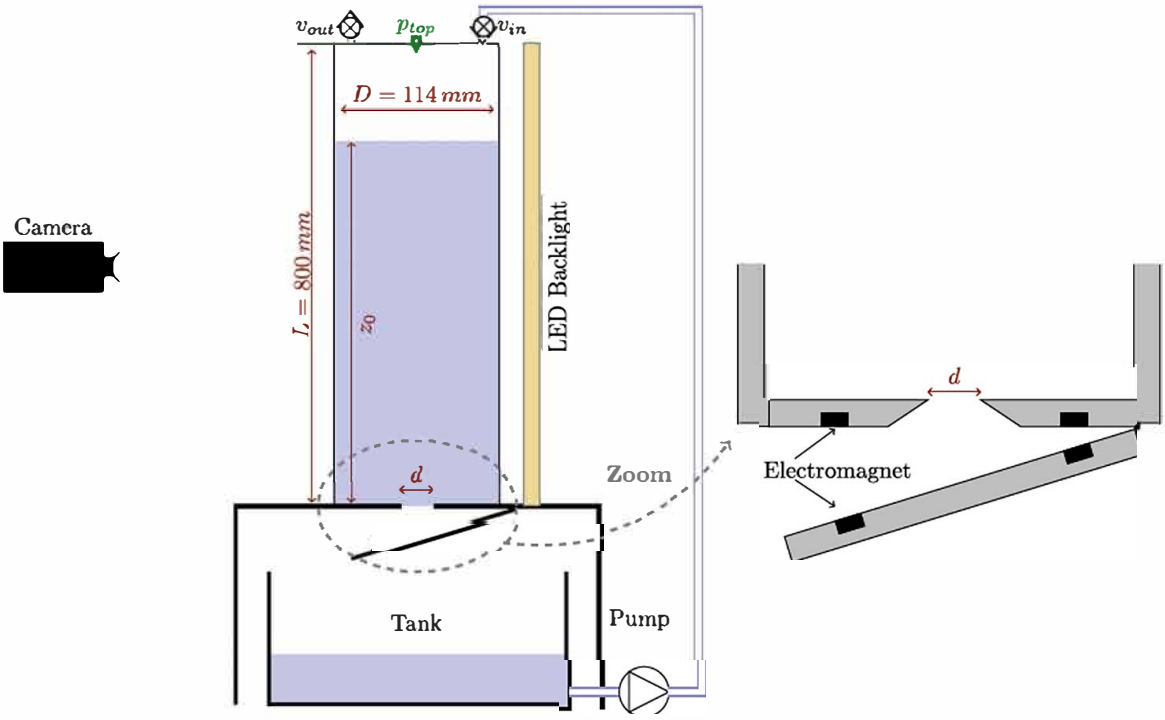

Fig. 1. Schematic of the experimental set-up and measurement means.

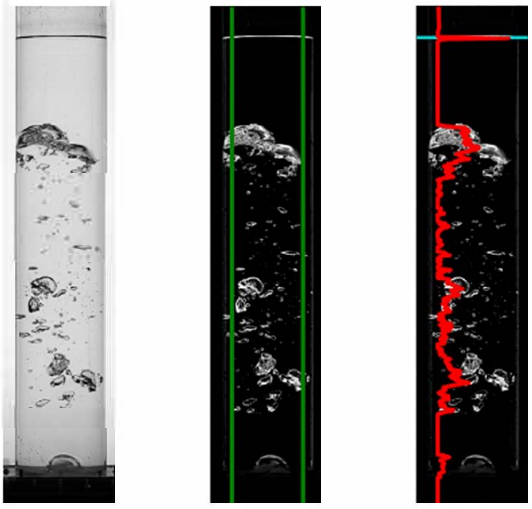

Fig. 2. The three successive steps in the image processing procedure for $d^* = 0.22$ and $\mathcal{F} = 0.75$. (a) Raw image; (b) image obtained after background removal; (c) vertical intensity profile (in red) obtained by averaging horizontally the pixel intensity between the two green lines in (b). The detection of the dominant peak makes it possible to follow the displacement of the upper free surface, indicated by the cyan line. (For interpretation of the references to colour in this figure legend, the reader is referred to the web version of this article.)

Corresponding data are acquired at a frequency $f_p = 1000$ Hz. Images of the emptying process are simultaneously recorded with a PCO™ Dimax camera with a full resolution of 2000×2000 pixels operating at a frequency $f_{im} = 200$ Hz. The cylindrical bottle is back-lighted by means of a LED panel (see Fig. 1). The camera and pressure sensor are synchronized through a TTL signal which also triggers the electromagnet, thus the gate opening.

Recorded images are post-processed to extract the vertical position, h_{int}, of the upper free surface. Fig. 2 displays each step of the image processing algorithm. First, a reference image, recorded before the beginning of the experiment, is subtracted from the raw image (a) to obtain the image (b). The latter displays a black background on which optical diopters, materializing gas-liquid interfaces, appear as gray shades since they are associated with a higher pixel intensity. The pixel intensity is averaged horizontally between the two green lines indicated on image (b) to construct the vertical intensity profile, displayed in red on image (c). Starting from the top, the first peak pinpoints the upper air-water interface. Thanks to an adaptive thresholding technique, the vertical position of this interface, indicated by the cyan line on image (c), is detected. At the beginning of the emptying process, when the free surface is flat and well defined (such as in Fig 2), the uncertainty in the determination of h_{int} is approximately 2 mm. Later, when large bubbles burst at the free surface, they generate a significant sloshing of the latter (e.g. in the right panel of Fig. 6). The uncertainty then increases significantly and is estimated, for late times and large openings, to be of the order of 20 mm.

A typical evolution of $h_{int}(t)$ is shown in Fig. 3 for $d^* = 0.22$ and $\mathcal{F} = 0.75$. This evolution reveals that the upper free surface moves down with a nearly constant speed throughout the emptying process, as previously observed by Kordestani and Kubie (1996) and CS. As shown in the inset of Fig. 3, the free surface position actually exhibits small oscillations superimposed on a regular evolution, owing to periodic ejection of liquid and bubble generation at the neck. The free surface position cannot be reliably detected at the very end of the process, owing to optical constraints. For this reason, all evolutions of $h_{int}(t)$ presented in the paper are truncated at a minimum value, $h_{int}/L = 0.06$.

3. Qualitative observations of the emptying process and two-phase flow structure

3.1. Successive stages of the emptying process

The emptying-generated flow may be seen as resulting from the coupling between two fluid systems triggered by the periodic

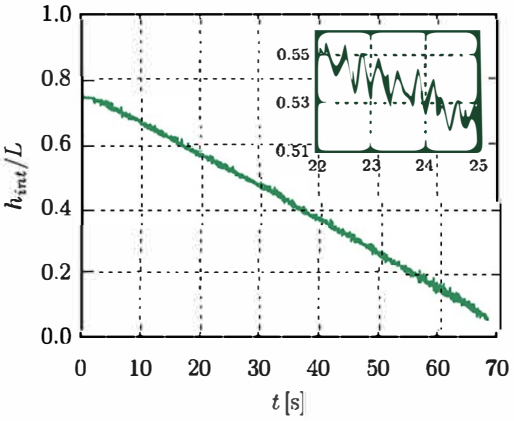

Fig. 3. Evolution of the position of the upper free surface during the emptying process for $d^* = 0.22$ and $\mathcal{F} = 0.75$. The inset provides a closer view at the oscillations of the free surface position during the time interval $22\,s \leq t \leq 25\,s$.

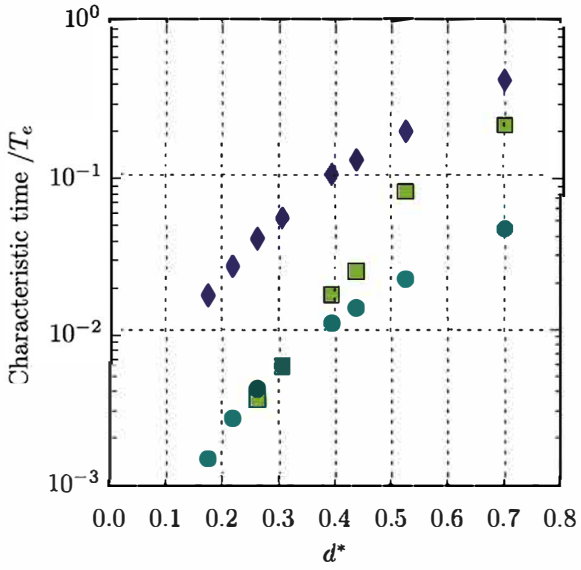

Fig. 4. Characteristic time scales of the three successive stages of the emptying process as a function of d^* for $\mathcal{F} = 0.77$. Green squares: τ/T_e; blue dots: T_{os}/T_e; purple diamonds: T_{fb}/T_e. Based on measurements, T_{os} was taken to be 0.2 s in all cases. (For interpretation of the references to colour in this figure legend, the reader is referred to the web version of this article.)

generation of air bubbles at the neck. The two systems, the top air buffer and the aerated water column, experience two successive transients before their coupling leads to a slowly-varying regime during which the pressure in the top air buffer oscillates periodically. Before the very first bubble generated at the neck reaches the top of the liquid column, the air buffer forms a closed gas volume. During this initial stage, a fast pressure transient with a characteristic decay time τ is detected within the buffer. Then, the first bubble reaches the water-air interface at time T_{fb}. After these transients, a slowly varying two-phase flow sets in and lasts until the emptying process is completed at time T_e. Throughout this 'fully-developed' stage, regular oscillations with period T_{os} are detected in the pressure signal recorded at the top of the bottle.

In the range of initial filling ratios investigated in the present study ($\mathcal{F} \geq 0.24$), all successive stages described above were always observed. Depending on the control parameters d^* and $\mathcal{F}$, the characteristic time ratios τ/T_e, T_{fb}/T_e and T_{os}/T_e may vary by more than one order of magnitude, as shown in Fig. 4. Selecting T_e as the reference time allows the relative duration of each stage of the evolution to be compared with the duration of the whole emptying sequence; any other choice did not provide a better scaling. Considering these large variations of the time ratios, it is likely that varying d^* and $\mathcal{F}$ yields contrasting flow dynamics. Whatever d^*, the period T_{os} is much smaller than the emptying duration T_e, implying that an oscillatory behavior takes place throughout the discharge, even with the largest necks. The characteristic time T_{fb} corresponding to the rise of the first bubble is approximately one order of magnitude larger than T_{os} whatever d^*. Hence, for large enough $\mathcal{F}$, before the first bubble reaches the upper free surface, several bubbles have entered the liquid column and may even have already broken up or coalesced. As d^* increases, T_{fb} may be up to 40% of T_e. Consequently, the transient stage lasts for nearly half of the total emptying time under such circumstances, and cannot be neglected. During such long transients, the first rising bubble is a large Taylor bubble, as shown in the right panel in Fig. 5. In contrast, short transients corresponding to small d^* involve much smaller, regularly spaced rising bubbles (left panel in Fig. 5). The specificities of these transients are discussed in more detail in Section 5. In Fig. 4, the damping time τ of the very first pressure transient is seen to vary from one-tenth to one-half T_{fb} when d^* increases. The various stages of the emptying process exist for all $\mathcal{F}$ as long as the initial volume of liquid is much larger than the volume of the first bubble emitted at the neck. However their relative duration may depend on the initial filling ratio, since their respective characteristic times vary differently with $\mathcal{F}$.

3.2. Overall evolution of the two-phase flow content

Fig. 6 displays images of the gas content in the water column at $t = 2.5$ s for normalized neck diameters ranging from $d^* = 0.18$ to $d^* = 0.7$. This time instant is typical of the slowly-varying regime that succeeds the initial transient. The cyan marker on each image corresponds to the detected free surface position. As expected, the larger the diameter of the opening is, the faster the cylinder empties. The flow dynamics may be characterized by a Reynolds number, $Re = V_e d/\nu_l$, based on the mean liquid velocity at the exit, V_e, and neck diameter, d. Since mass conservation implies that the emptying time, T_e, satisfies the equality $d^2 V_e T_e = \mathcal{F} L D^2$, the corresponding Reynolds number is $Re = \mathcal{F} L D^2/(\nu_l T_e d)$. In Fig. 6, Re ranges from 3000 for $d^* = 0.18$ to 22,500 for $d^* = 0.7$. Alternatively, one may define the Reynolds number $Re_D = d^* Re$ based on the cylinder diameter, D, and average emptying velocity, $\mathcal{F}L/T_e$. This Reynolds number ranges from 540 for $d^* = 0.18$ to 15,750 for $d^* = 0.7$. The Bond number, $Bo = \rho_l g d^2/\sigma$, with σ the water-air surface tension, of the large bubbles with a size of the order of d that form periodically at the neck is in the range 85–970, while their Weber number, $We = \rho_l V_e^2 d/\sigma$, is in the range 380–1200. Such bubbles are highly deformable and may break up easily, owing to the agitation of the high-Reynolds-number flow in the fluid column. It must be noticed that the dimensionless numbers Re, Bo and We characterizing the flow dynamics are independent on the initial filling ratio, $\mathcal{F}$.

Depending on the neck diameter, a broad variety of two-phase flow configurations is observed, ranging from isolated bubbles rising in a relatively quiescent ambient fluid - for small openings - to a flow which, qualitatively, looks like a chaotic foam when d^* gets close to unity. We did not observe any clear sharp transition from one flow regime to the other but rather a smooth and continuous variation with d^*. For a given d^*, we did not notice any significant effect of $\mathcal{F}$ on the observed flow regime provided $T_e >> T_{fb}$. For small opening diameters, typically $d^* = 0.18$ and 0.22, bubbles periodically generated at the bottom of the tank rise toward the free surface along oscillatory paths and only exhibit weak size variations. As the neck diameter increases, larger bubbles are generated. Although some of them may maintain their integrity throughout their rise, the majority undergoes successive 'catastrophic'

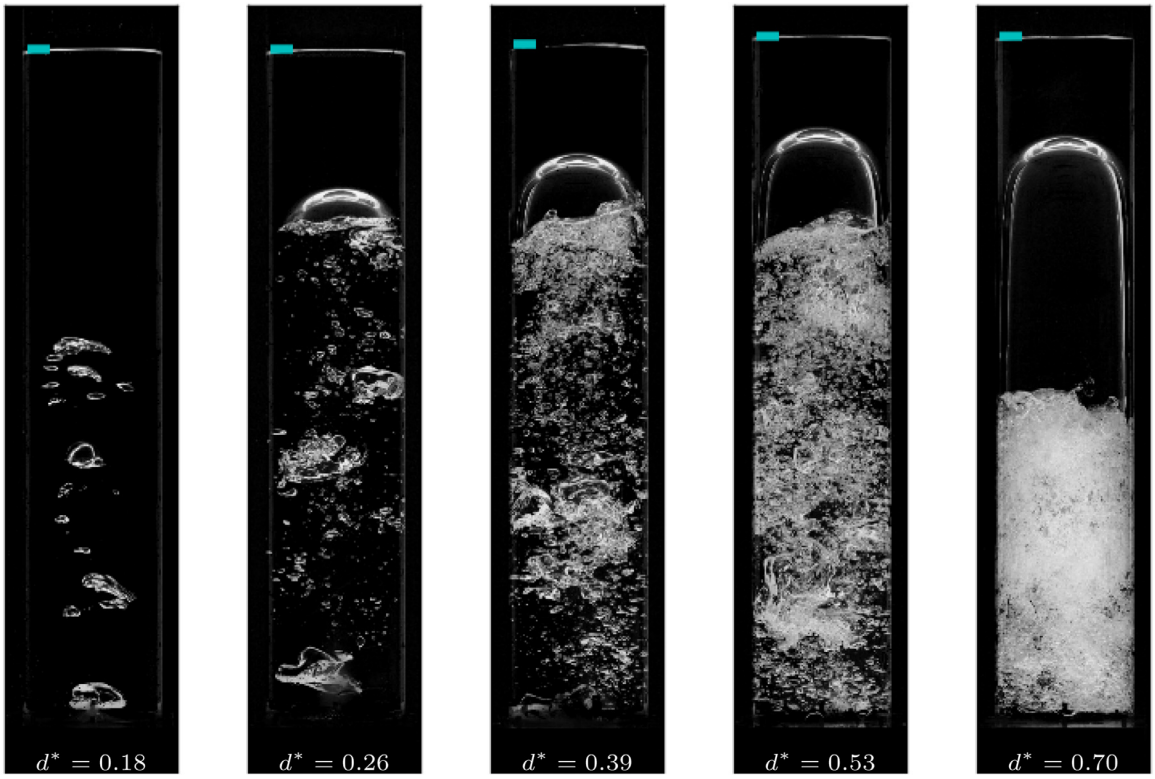

Fig. 5. Visualization of the gas content in the bottle during the initial transient ($t = 1.5\,\mathrm{s}$) for five different normalized neck diameters and the same initial filling, $\mathcal{F} = 0.77$. From left to right: $d^* = 0.18,\ 0.26,\ 0.39\,,0.53,\ 0.70$. The cyan marker in each panel indicates the detected free surface position. The computed mean gas volume fractions $\langle\alpha\rangle$ are $3, 6, 12, 17$ and 41%, respectively.

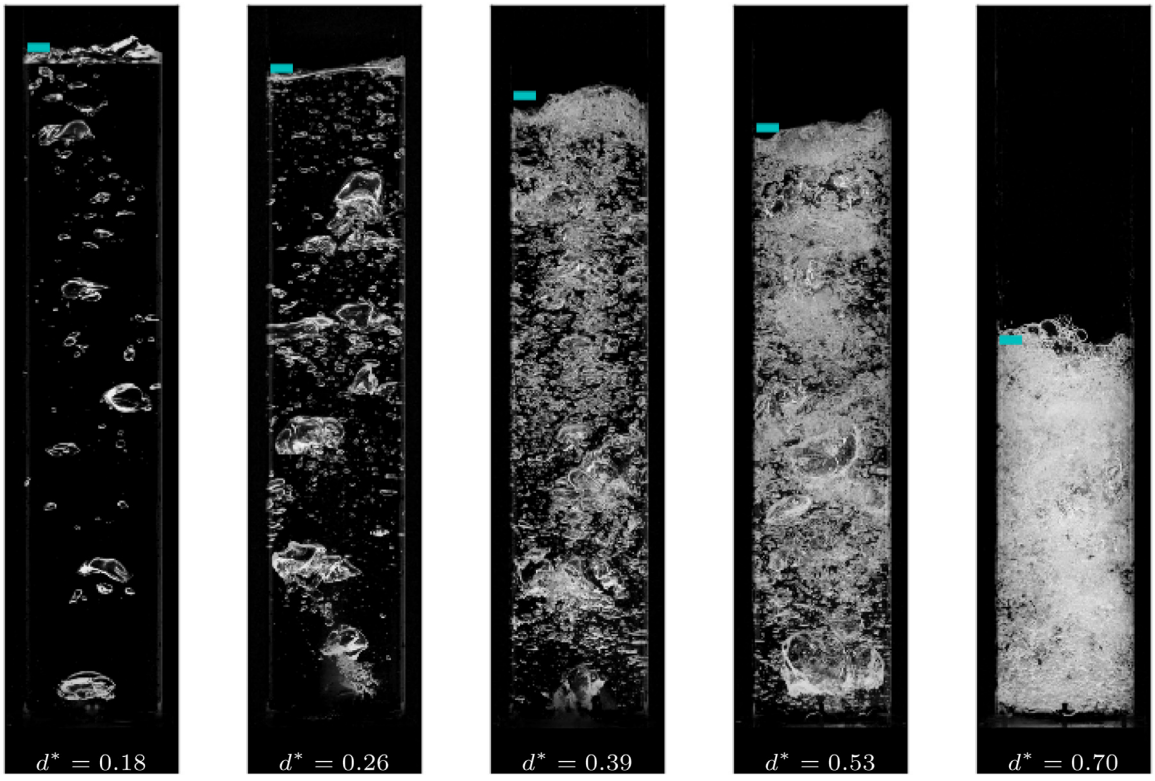

Fig. 6. Visualization of the gas content in the bottle in the fully-developed regime ($t = 2.5\,\mathrm{s}$) for the same five experiments as in Fig. 5. The corresponding computed mean gas volume fractions $\langle\alpha\rangle$ are $3, 5, 11, 16$ and 35%, respectively.

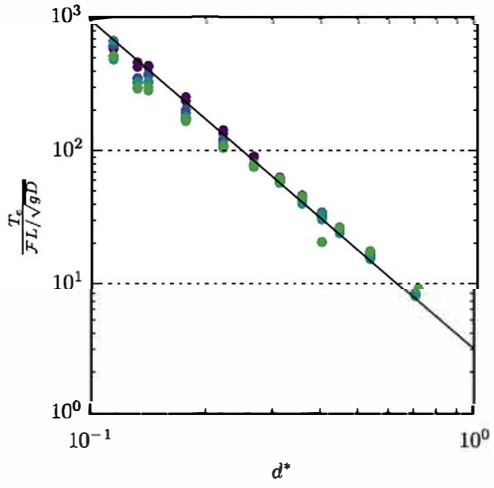

Fig. 7. Variation of the normalized emptying time, $T_e/(\mathcal{F}L/\sqrt{gD})$, with respect to the normalized neck diameter d^* for different initial filling ratios, $\mathcal{F}$. Each point gathers results obtained in several independent experiments. The color scale refers to the initial filling, with from dark to light: $\mathcal{F} = 1.0$, 0.74, 0.5 and 0.26. The solid line corresponds to the fit $T_e/(\mathcal{F}L/\sqrt{gD}) = 3.0\,d^{*\,5/2}$.

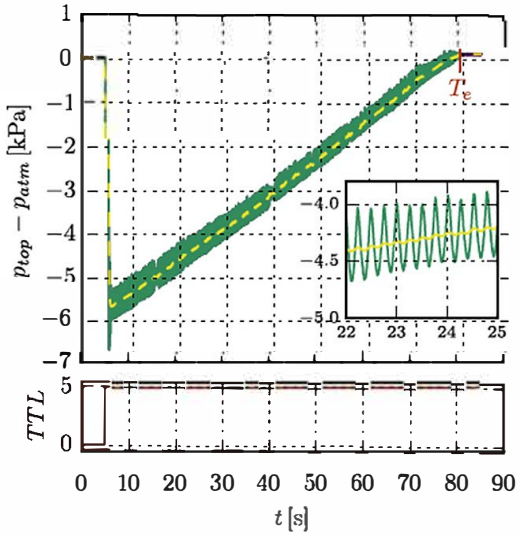

Fig. 8. Evolution of the pressure in the top air buffer for $d^* = 0.22$ and $\mathcal{F} = 0.75$, along with the TTL signal triggering the gate opening. The inset provides a closer view to the pressure oscillations during the time interval $22\,\mathrm{s} \le t \le 25\,\mathrm{s}$. Green: raw signal; yellow: Gaussian smoothing of the raw signal yielding the equilibrium pressure $\overline{p}_{top}(t)$. (For interpretation of the references to colour in this figure legend, the reader is referred to the web version of this article.)

reconfigurations and their average size decreases, owing to fragmentation. This yields a chaotic bubble swarm characterized by a broad bubble size distribution, as observed in Fig. 6 for $d^* \ge 0.39$. It is expected that this distribution broadens as Re is increased. Nevertheless, how its width and peak value vary with Re is unclear, since these characteristics are controlled by a complex combination of break-up and coalescence events. Despite the limitations of visual observation, Fig. 6 suggests that large bubbles and/or strong spatial modulations of the gas volume fraction, the extent of which increases with d^*, are present in the flow, at least up to $d^* = 0.53$. This provides evidence that the two-phase flow structure keeps some memory of the periodic gas injection at the neck.

Experimental observations at $t = 2.5$s suggest that the average gas volume fraction in the fluid column increases with the diameter of the opening. The quantitative determination of the space-averaged gas volume fraction, $\langle\alpha\rangle$, confirms this visual observation. More specifically, we find $\langle\alpha\rangle = 3$, 5, 11, 16 and 35% for $d^* = 0.18$, 0.26, 0.39, 0.53 and 0.70, respectively. Time variations of $\langle\alpha\rangle$ are analyzed in Section 4.4.

4. Macroscopic flow characteristics

4.1. Variations of the emptying time with the neck diameter and bottle filling ratio

The emptying time, T_e, defined as the time beyond which the measured pressure in the top air buffer, p_{top}, remains constant and equal to p_{atm}, decreases with both the neck diameter and the initial volume of water, as may be seen in Fig. 7. This figure gathers results obtained with various initial water heights and neck diameters (one point represents the result of several experiments). The theoretical prediction by CS is found to be in good agreement with observations. Hence, the model initially developed for $\mathcal{F} = 1$ may be extended to arbitrary initial filling ratios in the form

$$\frac{T_e}{3.0\,\mathcal{F}L/\sqrt{gD}} \approx d^{*-5/2}, \tag{2}$$

where $3.0\,L/\sqrt{gD}$ corresponds to the emptying time under conditions $d^* = 1$ and $\mathcal{F} = 1$ (Dumitrescu, 1943). Remarkably, the power law (2) holds from $d^* \approx 0.25$ to $d^* = 0.7$, and even down to $d^* = 0.11$ provided the initial filling ratio is large enough, typically $\mathcal{F} \gtrsim 0.75$. That this simple prediction holds throughout this wide range of relative openings and initial filling ratios indicates that the physical mechanisms governing the emptying process remain unchanged, despite the large differences in the flow structure observed in Fig. 6. For a given relative opening in that range, the emptying time increases linearly with the initial water volume in the bottle, itself proportional to $\mathcal{F}LD^2$. This observation suggests that no memory effect is involved in the overall emptying process, at least in the range of $\mathcal{F}$ investigated here. This trend is also consistent with the fact that the mean mass flux (which may be defined by applying a suitable sliding time average to the instantaneous liquid flow rate, see Section 4.2) remains constant throughout the discharge, as observed by Schmidt and Kubie (1995).

Deviations from linearity are noticed for $d^* \lesssim 0.25$ and $\mathcal{F} \lesssim 0.75$. For such small d^*, the smaller $\mathcal{F}$ the shorter the normalized emptying time, suggesting that T_e increases faster with $\mathcal{F}$ in that parameter range. As pointed out by CS, this is because the model neglects the liquid acceleration close to the opening and the nonlinearity of the pressure and velocity oscillations, both of which become increasingly important in the momentum balance as d^* and $\mathcal{F}L$ (i.e. the oscillating liquid mass) become small. As d^* further decreases, capillary effects come into play. Close to the blocking limit (observed to take place for $d^* \approx 0.07$, i.e. $d = 3\ell_c$, where $\ell_c = (\sigma/(\rho_l g))^{1/2} \approx 2.7$ mm is the capillary length), the emptying process exhibits an intermittent behavior due to the stabilizing influence of surface tension. While liquid ejection and bubble entrance alternate regularly most of the time, resting periods may take place without any regularity. Owing to this intermittency, the emptying time slightly varies from one experiment to another.

4.2. Evolution of the pressure in the top air buffer

The evolution of the pressure p_{top} in the air buffer is displayed in Fig. 8 for $d^* = 0.22$ and $\mathcal{F} = 0.75$. Starting with the initial value $p_{top} = p_{atm}$, the pressure immediately drops after the gate is opened. The pressure drop is close to the hydrostatic pressure variation corresponding to the height of the liquid column, $\rho_l g \mathcal{F} L$. Then, p_{top} increases almost linearly over time, until it recovers its initial value $p_{top}(0) = p_{atm}$ at the end of the discharge. A close view to the pressure signal (inset in Fig. 8) reveals that p_{top}

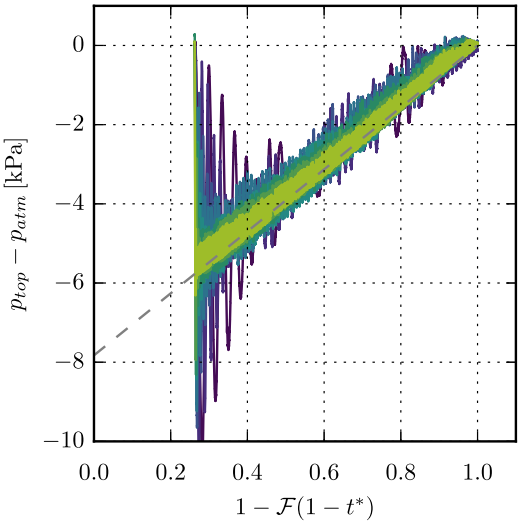

Fig. 9. Evolution of the pressure difference, $p_{top}(t) - p_{atm}$, vs. the normalized air volume in the bottle, for $\mathcal{F} = 0.74$ and various neck diameters. Each color line corresponds to a different neck diameter, with from dark to light: $d^* =$ 0.7, 0.53, 0.44, 0.39, 0.35, 0.31, 0.26, and 0.22. The dashed line represents the reference linear evolution of the hydrostatic component, $-\rho_l g \mathcal{F} L(1 - t^*)$.

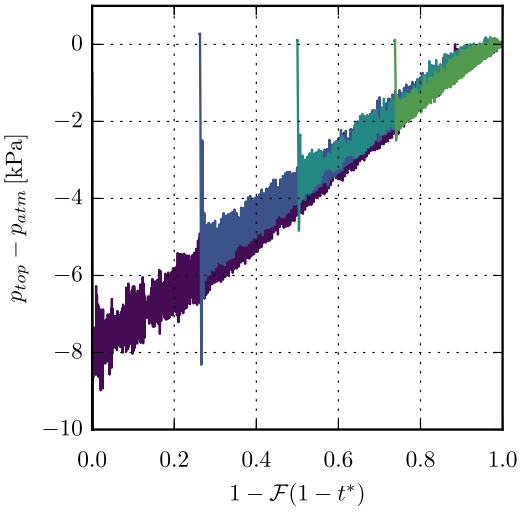

Fig. 10. Evolution of the pressure in the top air buffer, $p_{top}(t)$, vs. the normalized air volume in the bottle, for a normalized neck diameter $d^* = 0.31$ and various initial filling ratios. Each color line corresponds to a different initial filling ratio, with from dark to light: $\mathcal{F} = 1.0$, 0.74, 0.5, and 0.26.

oscillates about a slowly increasing value, $\overline{p}_{top}$, with a characteristic period $T_{os} \sim 0.2$ s, much shorter than the emptying time (the order of magnitude of which is $T_e \sim 75$ s in this case).

The slowly varying contribution $\overline{p}_{top}(t)$ is obtained by convoluting the pressure signal with a Gaussian kernel with a standard deviation $\sigma_G = 10/f_p = 0.01$ s. This pressure component corresponds to the equilibrium hydrostatic pressure, $p_{atm} - \rho_l g h_{int}(t)$, and obeys the relation

$$\overline{p}_{top}(t) - p_{atm} = -\frac{4}{\pi} \frac{g \overline{M}_w(t)}{D^2}, \tag{3}$$

where $M_w(t)$ is the remaining mass of water in the bottle at time t. In the present case, $\overline{p}_{top}(t)$ is found to evolve linearly, which indicates that the mean mass flow rate $-d\overline{M}_w/dt$ stays constant throughout the discharge.

As Fig. 6 revealed, the neck diameter has a deep influence on the structure of the two-phase flow throughout the emptying process. However, Fig. 9 shows that all pressure evolutions collapse on a master curve whatever d^*, provided time is rescaled appropriately. The suitable dimensionless time is $1 - \mathcal{F}(1 - t^*)$, with $t^* = t/T_e$, which corresponds to the normalized volume of air in the bottle at time t. Indeed this dimensionless time vanishes when the bottle is initially full of water and becomes unity at the end of the process when it is entirely filled with air. Existence of this master curve indicates that the slowly varying contribution $\overline{p}_{top}(t)$ grows linearly over time whatever d^*, and suggests that the physical mechanisms driving the long-term evolution of the emptying process are independent of d^*, in contrast with the average gas volume fraction $\langle \alpha \rangle$ which strongly depends on d^*. As Fig. 10 shows, the overall evolution of the slowly varying pressure component is also independent of the initial filling ratio. Nevertheless, the collapse is not perfect just after the opening. For all $\mathcal{F}$, $p_{top}(0) = p_{atm}$ but the return to the equilibrium pressure is essentially governed by effects of compressibility and depends on the initial volume of the air buffer, $1 - \mathcal{F}$. The duration of the transient (analyzed in more detail in Section 5.1) increases with the opening diameter, as already seen in Fig. 4. After this transient, the flow evolution no longer depends on the initial conditions.

The pressure oscillations that subsist at larger times represent the rapidly-varying contribution to the pressure signal. They are associated with the repeated occurrence of bubbles at the neck and crucially depend of the gas compressibility (Mer et al., 2018). We found the measured frequency, f_{os}, to be close to 5 Hz in all cases, with only a weak dependence on d^*. Moreover, f_{os} is in good agreement with the prediction of CS under all experimental conditions we considered. According to this prediction, the oscillation frequency depends on the gas thermodynamic characteristics and current water height as

$$f_{CS} = \sqrt{\frac{\gamma_{pv} p_{atm}}{\rho_g L^2}} \frac{\Phi}{\sqrt{\frac{h_{int}(t)}{L}\left(1 - \frac{h_{int}(t)}{L}\right)}}, \tag{4}$$

where Φ is a function that depends on $h_{int}(t)/L, d^*$ and D/L, ρ_g and γ_{pv} denoting the gas density and adiabatic index, respectively. That f_{os} is close to f_{CS} in all cases is noticeable, as part of our experiments are performed with opening ratios well beyond the maximum value $d^* = 0.44$ considered by CS. With such large openings, large Taylor bubbles dominate the initial transient, as seen in Fig. 5. A dense unsteady bubbly flow resulting from the quick break-up of the air volume entering the neck takes place in their wake. Despite this specific flow structure, which strongly differs from those observed with smaller d^*, f_{os} is still correctly approximated by (4) and remains in between 4 Hz and 5 Hz throughout the discharge.

Beyond the initial transient, pressure fluctuations gradually lose their left-right symmetry over a time period. This is especially true near the end of the discharge, in which the system involves strong nonlinear couplings. For this reason, we found appropriate to introduce a root mean square (rms) pressure fluctuation. This time-dependent fluctuation is defined as $p' = \langle (p_{top} - \overline{p}_{top})^2 \rangle_1^{1/2}$, where $\langle \cdot \rangle_1$ stands for a local time average over a 1 s window, i.e. approximately five oscillation periods. The evolution of p' beyond the initial transient is shown in Fig. 11 for neck diameters ranging from $d^* = 0.18$ to $d^* = 0.39$ and an initial filling ratio $\mathcal{F} = 0.74$. For large enough d^*, the emptying time becomes of the same order as the time window over which the average is performed. For this reason, the evolution of p' becomes meaningless for $d^* \gtrsim 0.39$. For lower d^*, the amplitude of pressure fluctuations is seen to increase with the neck diameter. This is because pressure oscillations in the air buffer are associated with the alternation of liquid ejections and bubble admissions through the neck (Mer et al., 2018), which makes their amplitude depend on the size of the generated bubbles, hence on d. Two successive stages may be identified in the

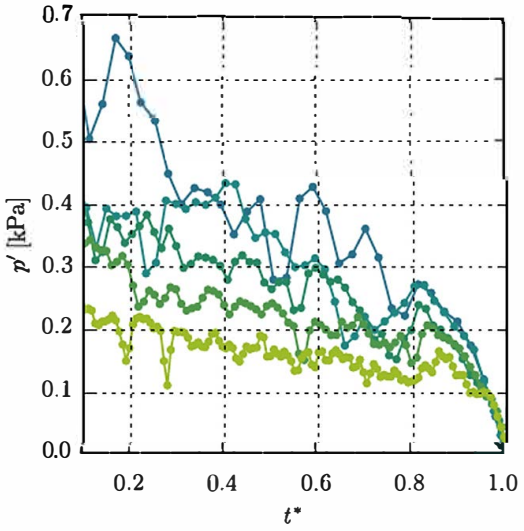

Fig. 11. Evolution of the rms pressure fluctuation p' for an initial filling ratio $\mathcal{F} = 0.74$ and various neck diameters. Each color line corresponds to a different neck diameter, with from dark to light: $d^* = 0.39$, 0.35, 0.31, 0.26 and 0.22.

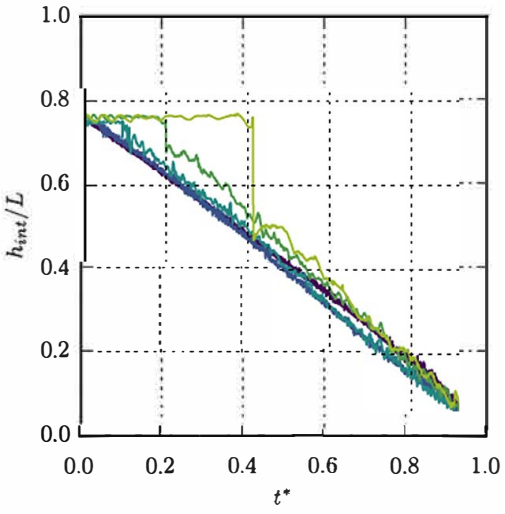

Fig. 12. Evolution of the normalized vertical position h_{int}/L of the upper free surface for various normalized neck diameters d^* and an initial filling ratio $\mathcal{F} = 0.77$. Each color line corresponds to a different neck diameter, with from light to dark: $d^* = 0.7$, 0.53, 0.39, 0.26 and 0.18.

evolution of p' for a given d^*. The first of them, up to $t^* \approx 0.8$, corresponds to a fully-developed regime characterized by a periodic generation of bubbles at the neck. During this stage, the amplitude of p' decreases almost linearly over time at a rate which increases with the neck diameter. For instance, p' decreases from 0.2 kPa at $t^* = 0.2$ to 0.1 kPa at $t^* = 0.8$ for $d^* = 0.22$, while it goes from 0.6 kPa to 0.35 kPa during the same time period for $d^* = 0.39$. The origin of this linear decrease is still unclear.

A second stage takes place for $t^* \gtrsim 0.8$, during which a rapid decrease of p' toward zero is observed. At the very end of the discharge, all p' evolutions collapse onto a single curve, indicating that the amplitude of pressure fluctuations no longer depends on the size of the opening. In this late stage, the separation of scales between the water height, h_{int}, and the neck diameter, d, no longer holds. A strong coupling between the bubble release at the neck and the displacement of the free surface takes place (see movies accompanying the paper).

4.3. Descent of the free surface

The evolution of the upper free surface position is shown in Fig. 12 for various neck diameters and an initial filling ratio $\mathcal{F} = 0.77$. Two distinct stages are observed when $d^* \geq 0.26$. In the first of them, the position of the free surface remains roughly constant, i.e. the water height does not vary. Small-amplitude oscillations about this position are nonetheless observed but these oscillations are quickly damped. This first stage coincides with the rise of the first air bubble through the water column. The volume of this leading bubble, together with that of the swarm of smaller bubbles in its wake (see Fig. 5), compensates for the volume of liquid that exits from the bottle, leaving h_{int} unchanged. When the first bubble reaches the free surface and becomes part of the air buffer, the volume of the latter increases suddenly. Consequently, $h_{int}(t)$ exhibits a downward step right at this instant, as Fig. 12 confirms. This event does not affect the exiting liquid flow rate. The duration of this first stage is determined by the time T_{fb} required for the first bubble to reach the free surface, which, in a first approximation, increases linearly with $\mathcal{F}$, similar to T_e. For $\mathcal{F} = 0.77$, this time is found to be constant and of the order of 1.9 s for $d^* \geq 0.31$, which shows that the rise speed of the corresponding bubble is independent of d^* when the diameter of the opening is large enough. Lower d^* yield slightly larger T_{bf}. The height of the h_{int}-step is governed by the bubble volume and is of the order of 30 mm for $d^* = 0.39$, increasing to 200 mm for $d^* = 0.70$. The height of the step is expected to increase with $\mathcal{F}$, since increasing the initial filling rate increases the time available for coalescence events to occur at the back face of the leading bubble (see Section 5.2). This first stage exists for all neck diameters. However, for $d^* \lesssim 0.2$, its duration and the height of the step become much smaller than T_e and $\mathcal{F}L$, respectively, which makes them too small to be identified in Fig. 12.

In the next stage, the free surface descent is characterized by a constant velocity. Its evolution follows the simple law

$$h_{int}(t)/L = \mathcal{F}\,(1 - t^*)\,. \tag{5}$$

Using (2), the vertical velocity of the free surface is then found to obey

$$\frac{U_{fs}}{\sqrt{gd}} \approx \frac{1}{3} d^{*2}\,. \tag{6}$$

It increases with the relative diameter of the opening, from 5 mm s^{-1} for $d = 20$ mm to 145 mm s^{-1} for $d = 80$ mm.

4.4. Mean gas volume fraction in the fluid column

From the equilibrium pressure and the position of the free surface, we can estimate the mean gas volume fraction in the fluid column as

$$\langle\alpha\rangle = 1 - \frac{p_{atm} - \overline{p}_{top}}{\rho_l g \overline{h}_{int}}\,, \tag{7}$$

where $\overline{h}_{int}$ is the equilibrium height of the column determined by convoluting the signal $h_{int}(t)$ with a Gaussian kernel. The accuracy in the determination of $\langle\alpha\rangle$ is directly related to that in the detection of the free surface height, i.e. $\Delta\alpha \sim \alpha \Delta\overline{h}_{int}/\overline{h}_{int}$. We quantified the corresponding uncertainty by examining the interfacial region on a selection of raw images and considering how $\overline{h}_{int}$ is affected by local fluctuations. The estimated uncertainty was found to be negligible at the beginning of the emptying process but increases significantly when the interface gets closer to the neck. For $t^* \approx 0.8$, considering $\Delta\overline{h}_{int} \approx 2$ cm, $\overline{h}_{int} \approx 16$ cm and $\alpha \approx 0.3$, the uncertainty on α is estimated to be of the order of 0.04, i.e. $\Delta\alpha/\alpha \approx 12\%$. We used the measurement technique described in Section 2.2 to determine the evolution of $\langle\alpha\rangle$ for various neck diameters (the

photographs displayed in Figs. 5 and 6 provide snapshots of the corresponding flows). This evolution is shown in Fig. 13, using the normalized time t^*. Again we identify the two distinct regimes observed in Fig. 12. That is, the gas volume fraction first increases linearly, which corresponds to the liquid being ejected from the bottle and replaced by an equivalent volume of gas. Once the first bubble has reached the free surface, less gas remains entrapped within the fluid column, which leads to a sudden decrease of $\langle\alpha\rangle$. For $d^* = 0.7$, the burst of the first bubble occurs at $t^* = 0.4$ and yields a 50% reduction of $\langle\alpha\rangle$. This phenomenology takes place for all neck diameters, as testified by the presence of a kink in all four evolutions of $\langle\alpha\rangle$ corresponding to $d^* \geq 0.39$ in Fig. 12. Nevertheless, for $d^* \lesssim 0.3$ the volume of the bubble that first reaches the free surface is too small to leave a signature in Fig. 13.

Beyond this first stage, the mean gas volume fraction continuously increases over time at a rate which also goes on increasing. This is because most of the large bubbles contained within the fluid column break up into a large number of smaller bubbles as they rise. Small bubbles having a significantly lower rise speed than large ones, the volume occupied by the gas phase increases during the emptying process. In addition, as the discharge goes on, the overall agitation in the fluid increases. Indeed, the first bubbles generated at the neck rise in a relatively quiet water column in which the fragmentation rate is low. In contrast, the subsequent large air bubbles evolve within a much more agitated medium in which fragmentation is more likely to occur. This enhanced agitation concurs to produce smaller bubbles which stay longer within the fluid column, making the rate of change of $\langle\alpha\rangle$ increase throughout the process.

Fig. 13 indicates that $\langle\alpha\rangle$ is an increasing function of the relative neck diameter whatever t^*. This feature is a direct consequence of the relative volume of bubbles generated at the neck with frequency f_{os}, which grows like d^{*3}. Nevertheless, rescaling the experimental curves by d^{*3} does not make them collapse on a single master curve. The reason for this may be revealed by setting up a simple model allowing the observed evolutions to be predicted beyond the initial transient, assuming negligible compressibility of the gas within the two-fluid column. The evolution of the gas volume fraction within the column is driven by the difference between the air flux entering through the neck, q, and the one leaving through the upper free surface, $Q = \pi D^2 U_{fs}/4$. The gas flux at the neck is approximately $q = \zeta \pi d^3/(6T_{os})$, where ζ is an $\mathcal{O}(1)$ pre-factor characterizing the actual size of bubbles detaching from the neck. For a given discharge, we keep ζ constant, just as T_{os} (see Section 4.2). Beyond the initial transient, the volume of the two-phase column evolves as $\mathcal{V}_{tp}(t) = \pi D^2/4\big(\mathcal{F}L - U_{fs}t\big)$. Equating the time rate-of-change of the gas volume within the column, $\langle\alpha\rangle_m(t)\mathcal{V}_{tp}(t)$, with the difference between the entering and leaving gas fluxes and integrating over time yields the predicted gas volume fraction $\langle\alpha\rangle_m$ as

$$\langle\alpha\rangle_m = \alpha_0 + \frac{\frac{2}{3}\zeta d^{*3} D/T_{os} - U_{fs}}{\mathcal{F}L - U_{fs}t}(t - t_0)\,, \tag{8}$$

where α_0 is the initial volume fraction which we set to the measured $\langle\alpha\rangle$ at $t = t_0 = 2\,\mathrm{s}$, since the model does not account for the formation of the bubble swarm during the initial stage $t < t_0$. The pre-factor ζ is obtained through a least-square fit of the experimental data. Model predictions are compared with experimental evolutions in Fig. 14, revealing a good agreement for $d^* < 0.35$. For larger diameters, the predictions deteriorate, presumably as a consequence of the higher level of agitation within the fluid column. More specifically, owing to this intense agitation, fragmentation produces a larger number of small bubbles. A significant fraction of them never reaches the top air buffer, as the corresponding bubbles are entrained downwards by the outgoing liquid and eventually ejected through the neck.

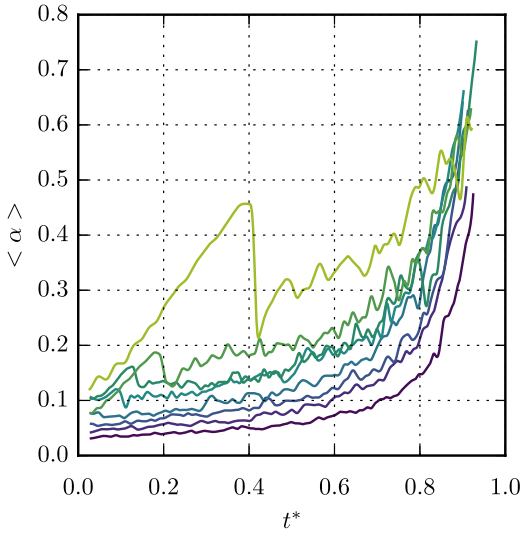

Fig. 13. Evolution of the space-averaged air volume fraction, $\langle\alpha\rangle$, in the fluid column for $\mathcal{F} = 0.77$ and various normalized neck diameters, d^*. Each color line corresponds to a neck diameter, with from light to dark: $d^* = 0.7$, 0.53, 0.44, 0.39, 0.31, 0.26, 0.22 and 0.18.

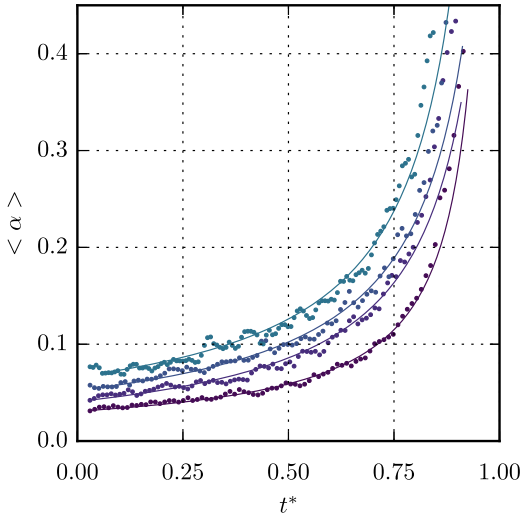

Fig. 14. Assesment of the space-averaged air volume prediction (8) for the four smallest d^* displayed in Fig. 13. The solid lines and dots refer to $\langle\alpha\rangle_m$ and $\langle\alpha\rangle$, respectively.

5. Early times of the discharge

5.1. Pressure transient

The transition from the initial state in which the pressure in the air buffer equals the atmospheric pressure, to the regime in which it gradually oscillates around a slowly-evolving equilibrium hydrostatic component, is illustrated in Fig. 15 for $d^* = 0.44$ and $\mathcal{F} = 0.75$. This transient is characterized by an exponential decay of the amplitude of oscillations, until they reach a slowly-varying amplitude of the order of 1 kPa. This initial transient may be seen as the impulse response of the system to the pressure disturbance generated by the initial condition, here the sudden gate opening.

As shown in Fig. 15, the amplitude of pressure oscillations is accurately fitted with an exponential function of the form $Ae^{-t/\tau} + B$, where τ is the characteristic decay time, A the initial amplitude of oscillations and B their amplitude at the beginning of the slowly-evolving regime. Care must be taken when applying such a

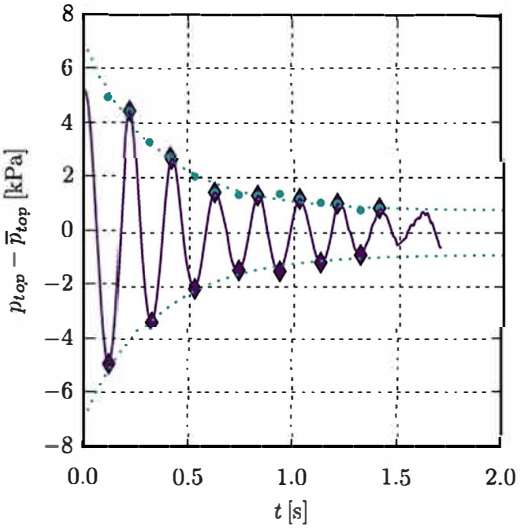

Fig. 15. Pressure oscillations during the initial transient for $d^* = 0.44$ and $\mathcal{F} = 0.75$. Solid line: recorded amplitudes; diamonds: extrema of oscillations; dots: absolute value of the extrema used in the fitting procedure; dotted line: fitting curve $Ae^{-t/\tau} + B$, with $A = 6.2$ kPa, $\tau = 0.34$ s and $B = 0.8$ kPa.

nonlinear fitting procedure on a scarce data set. For small neck diameters, below $d^* \approx 0.26$, the damping time is of the same order as the oscillations period and therefore can not be accurately estimated. This is why only neck diameters $d^* \geq 0.26$ are considered in this section. Values of B agree qualitatively with the experimental determinations of p' reported in Section 4.2 at the beginning of the slowly-evolving regime.

The amplitude of oscillations, normalized by the hydrostatic pressure difference, $\rho_l g \mathcal{F} L$, is displayed in Fig. 16 (left). This figure shows that A is entirely determined by the initial conditions - the pressure $p_{top}(0) = p_{atm}$ in the air buffer and the filling ratio $\mathcal{F}$ - and does not depend on d^*. In contrast, the neck diameter deeply influences τ, which increases from 0.18 s for $d^* = 0.26$ to 0.92 s for $d^* = 0.7$. Considering a power law $\tau \propto d^n$, n is found to vary from $n \approx 1.3$ for $d^* \lesssim 0.4$ to $n \approx 1.7$ for $d^* = 0.7$. which suggests that τ is approximately proportional to $d^{3/2}$ throughout the whole range of neck diameters. Note that this exponent is clearly lower than $n = 2$, ruling out the intuitive idea that the decay might be related to viscous effects in the neck region, in which case τ would scale as d^2/ν_l. The $d^{3/2}$-scaling may be understood by considering that the deformability of the first bubbles entering the water column damps the initial pressure oscillation by converting part of the corresponding energy into interfacial energy of gas-liquid interfaces. To put this scenario on a firmer basis, consider the isolated system made of the air buffer+liquid column, before the very first bubble detaches from the neck and the very first liquid jet is ejected outwards. Assuming the liquid to be incompressible, the mechanical work in this system results solely from the action of the pressure within the air buffer with volume $\mathcal{V}_{ab}(t)$, and makes the bulk internal energy vary by $-p_{top}(t)d\mathcal{V}_{ab}$ when the buffer volume varies by $d\mathcal{V}_{ab}$. Assuming that the upper free surface remains flat, i.e. its area does not vary, the surface energy $\sigma \mathcal{A}_b(t)$ associated with air-water interfaces involved in the system varies by $\sigma d\mathcal{A}_b$, owing to the work of surface tension resulting from interfacial area variations in the neck region. If dissipation were negligible in this system, the internal energy of the whole system would be conserved, implying that the negative work corresponding to an expansion of the air buffer would be exactly balanced by a positive work resulting from an increase of the interfacial area in the neck, such that $\sigma d\mathcal{A}_b(t) = p_{top}(t)d\mathcal{V}_{ab}$. This is where the neck diameter enters the scaling of the decay time τ. Keeping in mind that the capillary time at the neck scales as $\rho_l d^3/\sigma$, we normalize τ by $2\pi/\omega_2$, where ω_2 stands for the radian frequency of the lowest mode of capillary oscillations of a nearly-spherical bubble with diameter d (so-called $l = 2$ mode), known to be $\omega_2 = \left(96\sigma/(\rho_l d^3)\right)^{1/2}$ (Lamb, 1932). As Fig. 16 (right) shows, τ is adequately re-scaled in this way, although some scatter remains, and the dimensionless decay time $\omega_2 \tau / 2\pi$ is of $\mathcal{O}(1)$ as expected.

The initial transient may be considered to end at $t \approx 2.5\,\tau$, for which $e^{-t/\tau} \approx 0.08$. According to Fig. 4, the time T_{fb} at which the first bubble reaches the upper free surface exceeds $2.5\,\tau$ for all neck diameters such that $d^* \lesssim 0.5$. For $t < T_{fb}$, the air buffer behaves as a closed thermodynamic system with a constant mass. Its volume, $\mathcal{V}_{ab}(t) = \frac{\pi D^2}{4}(L - h_{int}(t))$, is known from the record of the free surface position $h_{int}(t)$. Taking into account the initial condition $p_{top}(0) = p_{atm}$ and assuming that air behaves as an ideal gas, we computed pressure variations in the air buffer during the whole transient using the recorded variations of $\mathcal{V}_{ab}(t)$, after postulating either an isothermal or an isentropic evolution, the latter with an adiabatic index $\gamma_{pv} = 1.4$.

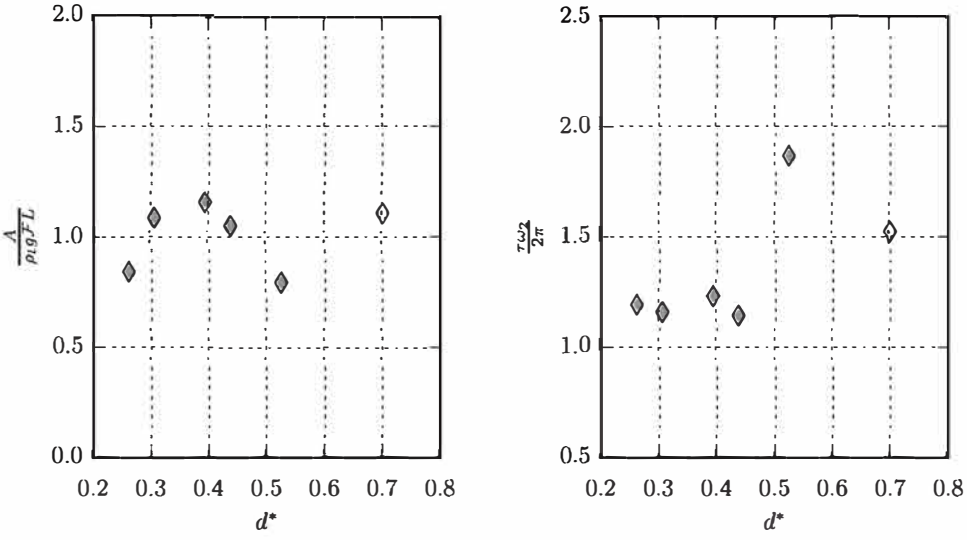

Fig. 16. Variation of the normalized amplitude $\frac{A}{\rho_l g \mathcal{F} L}$ of pressure oscillations (left), and decay time $\frac{\omega_2 \tau}{2\pi}$ of the pressure transient (right), with respect to the normalized neck diameter d^*.

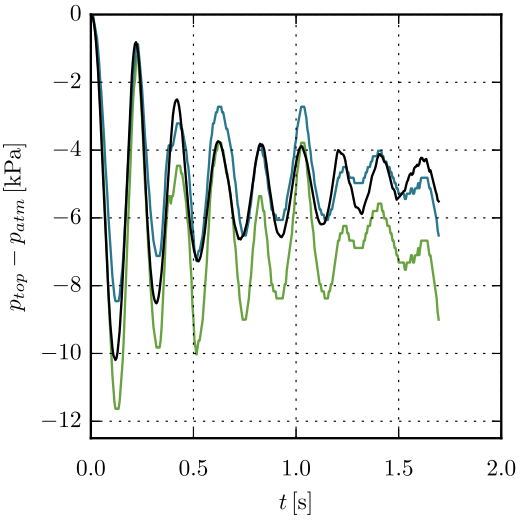

Fig. 17. Evolution of the pressure in the air buffer during the first two seconds for $d^* = 0.44$ and $\mathcal{F} = 0.75$. Black: recorded signal; green and blue: predicted evolution assuming isentropic and isothermal evolutions, respectively. (For interpretation of the references to colour in this figure legend, the reader is referred to the web version of this article.)

As Fig. 17 reveals, the actual pressure evolution stands in between these two extreme assumptions, but significantly closer to the isothermal evolution. A similar comparison was carried out for all exit diameters, leading to the same conclusion. This implies that, following the scenario discussed above, only part of the work resulting from the displacement of the upper free surface is converted into surface energy at the neck, while the rest is dissipated in the bulk and at the walls. As an aside, the fact that the pressure prediction based on the experimental determination of $h_{int}(t)$ is consistent with the recorded signal $p_{top}(t)$ also provides an indirect check of the consistency of the pressure and free surface height measurements.

5.2. First rising gas entity

The evolution of the gas volume fraction discussed in Section 4.4 revealed the influence of the first rising gas entity (hereinafter abbreviated as FRGE) on the global evolution of the system, most notably for large d^*. This entity differs from all bubbles subsequently emitted at the neck, as it is the only one that rises in a quiescent liquid. This distinctive condition deeply affects its shape, stability and rise speed. To get more insight into these features, the interface height detection algorithm described in Section 2.2 was adapted to also detect the second peak present in the vertical pixel intensity distribution, as it corresponds to the apex of the FRGE. The position of the tail of the FRGE was also detected in configurations with $d^* \geq 0.44$. Fig. 18 shows how the geometry of the FRGE varies with the neck diameter by the time its apex reaches the median horizontal plane of the bottle. In this figure, the initial filling rate is kept fixed, with $\mathcal{F} = 0.77$.

Whatever $d^* > 0.18$, it turns out that the FRGE takes the form of a spherical cap bubble or a Taylor bubble, the volume of which significantly increases with d^*. When $d^* \geq 0.39$, the length-to-diameter ratio of the Taylor bubble is of $\mathcal{O}(1)$ or more. The apex rise speed, V_{ap}, was calculated for vertical positions $0.44 \leq z/L \leq 0.69$, then averaged over this range. Fig. 19 shows that $V_{ap} \approx 0.36\,\mathrm{m\,s^{-1}}$ whatever d^*. Based on this estimate, the characteristic Reynolds number of the FRGE, $Re_{ap} = V_{ap}D/(2\nu_l)$, is approximately 2×10^4. Spherical cap bubbles rising in an

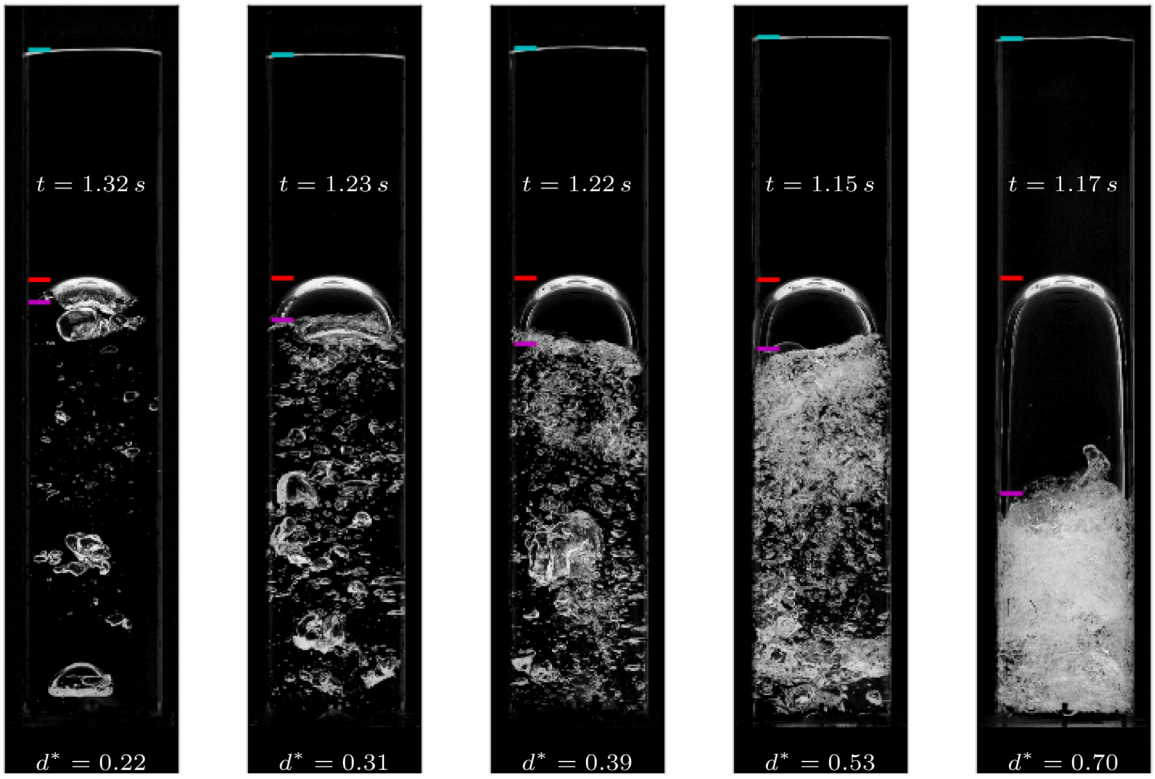

Fig. 18. Visualization of the first rising gas entity (FRGE) by the time its apex reaches the vertical position $h/L = 0.5$, for $\mathcal{F} = 0.77$ and various neck diameters. The time required for the FRGE to reach $h/L = 0.5$ is specified in each image. The cyan, red and magenta lines indicate the detected free surface, FRGE apex and back face position, respectively. The configuration corresponding to $d^* = 0.18$ was not reported because the coalescence rate is too low for bubbles periodically emitted at the neck to generate a spherical cap bubble.

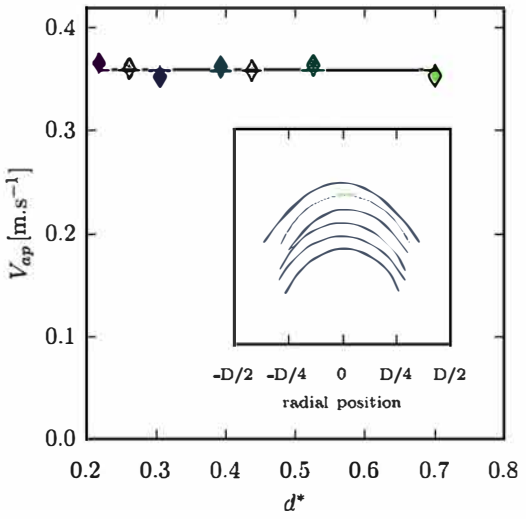

Fig. 19. Rise speed of the FRGE apex for various normalized neck diameters. Solid line: $V_{ap} = 0.34\sqrt{gD}$. Inset: shape of the front part of the corresponding FRGE in Fig. 18 with, in black, the leading-order term $r = \sqrt{Dz_{ap}}$ in the potential flow solution (lines have been shifted vertically to improve readability, and horizontally to make the apex coincide with the tube axis in all cases). Colors specify the correspondence between the front shape (inset) and the rise speed (top curve), with from dark to light: $d^* = 0.22$, 0.31, 0.39, 0.53 and 0.70.

unbounded domain or in tubes have been widely studied since Dumitrescu (1943) and Davies and Taylor (1950) (who considered bubble sizes yielding Reynolds numbers up to $Re_{ap} \approx 1.2 \times 10^4$); see the reviews by Wegener and Parlange (1973) and Fabre and Liné (1992). The bubble rise speed is known to scale with the square root of the curvature radius at the apex. That V_{ap} is independent of d^* suggests that all bubbles have a similar curvature in present experiments. This is confirmed in the inset of Fig. 19, where we superimposed all front shapes corresponding to bubbles shown in Fig. 18, extracted by a contour detection algorithm. The crucial role of confinement by the lateral wall is emphasized by the leading-order potential flow solution, which predicts the shape in the apex region to be close to $r = \sqrt{Dz_{ap}}$, with z_{ap} the vertical distance from the apex (Davies and Taylor, 1950; Héraud, 2002; Clanet et al., 2004). This solution makes it clear that the bubble shape, hence V_{ap}, does not depend on d^*.

A minimum gas volume must be present in the two-phase column for a spherical cap or Taylor bubble to form. This critical volume is available since the very first bubble forms at the neck for large enough d^*. Conversely, it is reached only after several coalescence events for small neck diameters (see the accompanying movies and compare those corresponding to $d^* = 0.18$ and 0.31). This is why no spherical cap bubble was observed with $d^* = 0.18$, owing to the insufficient number of such events allowed by the limited height of the device. That successive coalescence events are required to generate a spherical cap bubble has an influence on the time required for the FRGE to reach a given vertical position. As Fig. 18 indicates, this time increases with decreasing d^*, in line with the smaller coalescence rate observed for small d^*.

A simple model may be set up to get some insight into the growth of the Taylor bubble due to the coalescence of small bubbles at its back. The idea is to consider the fluid column with volume $\mathcal{V}_{tp} = \pi D^2 \mathcal{F} L/4$ at the bottom of which small bubbles are injected periodically, and examine the gas flow rate exchanged between the two markedly different bubbles populations present in this column, namely the large spherical cap or Taylor bubble and the swarm of small bubbles. The large bubble is characterized by the vertical position of its apex, $h_{ap}(t)$, and back face, $h_{ba}(t)$. As shown in Fig. 20 (left), these positions evolve with different speeds, depending on d^*. Based on these two positions, the volume of the large bubble, $\mathcal{V}_T$, may be approximated by considering that it consists of a half sphere and a cylinder, so that $\mathcal{V}_T = \pi D^2/4\left(h_{ap} - h_{ba} - D/2\right) + \pi D^3/12$. Small bubbles are located in the rear volume, $\mathcal{V}_r = \pi D^2 h_{ba}/4$, and occupy an actual volume $\mathcal{V}_{sw} = \langle\alpha_{sw}\rangle \mathcal{V}_r$, where $\langle\alpha_{sw}\rangle$ denotes the gas volume fraction in the swarm. Knowing the two positions, $h_{ap}(t)$ and $h_{ba}(t)$, the total volume of the column, $\mathcal{V}_{tp}(t)$, and the global gas volume fraction, $\langle\alpha\rangle(t)$, makes it possible to determine $\mathcal{V}_{sw} = \langle\alpha\rangle \mathcal{V}_{tp} - \mathcal{V}_T$, hence $\langle\alpha_{sw}\rangle = \mathcal{V}_{sw}/\mathcal{V}_r$. The evolution of $\langle\alpha_{sw}\rangle(t)$ is reported in Fig. 20, where it may be compared with that of $\langle\alpha\rangle(t)$ which rises linearly during this stage. As time proceeds, the swarm volume fraction exhibits a clear decrease on which oscillations resulting from fluctuations (especially along the lateral wall) in the position of the back face of the large bubble superimpose. These fluctuations reflect the chaotic sloshing of this back face induced by the burst of trailing bubbles. To overcome the corresponding large potential uncertainty in the measurement of $h_{ba}(t)$, we fitted the data so as to retain only the dominant trend in each series. It is noteworthy that for $t \to T_{fb}$, $\langle\alpha_{sw}\rangle(t)$ consistently decreases down to values close to those measured for $\langle\alpha\rangle(t)$ right after $t = T_{fb}$ (Fig. 13), as conservation of the gas volume requires. Assuming that bubbles periodically injected at the neck feed the swarm of small bubbles but not the large bubble itself because its back face stands already far from the neck during the sequence under consideration ($h_{ba} \geq 15$ cm according to Fig. 20), we may write

$$\frac{d\mathcal{V}_T}{dt} = \mathcal{C}_{sw\to T}\,, \tag{9}$$

$$\frac{d\mathcal{V}_{sw}}{dt} = \mathcal{S}_e - \mathcal{C}_{sw\to T}\,, \tag{10}$$

where $\mathcal{S}_e$ is the source term resulting from the periodic admission of air at the neck, and $\mathcal{C}_{sw\to T}$ is the volume flow rate exchanged between the swarm and the large bubble, owing to coalescence and break-up events happening in the wake of the latter. Using linear or cubic polynomial fits of $h_{ap}(t)$, $\langle\alpha\rangle(t)$ and $h_{ba}(t)$, especially to remove fluctuations in the latter, (9) and (10) may be employed to determine the source/sink terms $\mathcal{S}_e(t)$ and $\mathcal{C}_{sw\to T}(t)$. Corresponding predictions are reported in Fig. 20. The prediction for $\mathcal{S}_e$ is found to be within 10% of the expected theoretical value, $\pi d^3/(6T_{os})$, giving credit to the post-processing procedure. The exchange term $\mathcal{C}_{sw\to T}(t)$ is always positive, which ensures the growth of the Taylor bubble. In all cases, $\mathcal{C}_{sw\to T}$ is initially larger than $\mathcal{S}_e$. Presumably, the reason why the coalescence rate is so large during this very early stage stands in the strong acceleration experienced by small bubbles entrapped in the wake of the large bubble and sucked toward its back face. Due to the imbalance between $\mathcal{C}_{sw\to T}(t)$ and $\mathcal{S}_e(t)$ at early time, the gas volume in the swarm decreases, despite the gas flow rate entering the column. As the large bubble rises, $\mathcal{C}_{sw\to T}(t)$ decreases, making $\langle\alpha_{sw}\rangle$ vary much more slowly. As Fig. 20 shows, the larger d^*, the higher the initial value of $\mathcal{C}_{sw\to T}(t)$ is. This is why the final volume of the Taylor bubble increases with the normalized neck diameter, as does the magnitude of the jump experienced by the free surface and the gas volume fraction at $t = T_{fb}$ (Figs. 12 and 13).

6. Summary and concluding remarks

This study provides new experimental insights into the flow resulting from the emptying of a vertical cylindrical bottle initially filled with water up to a certain level. The oscillatory nature of this flow, resulting from the coupling between the compressible top air buffer and the two-phase column crossed by gas bubbles generated at the neck, was examined in detail by CS. Present experiments were performed with similar neck-to-cylinder diameter

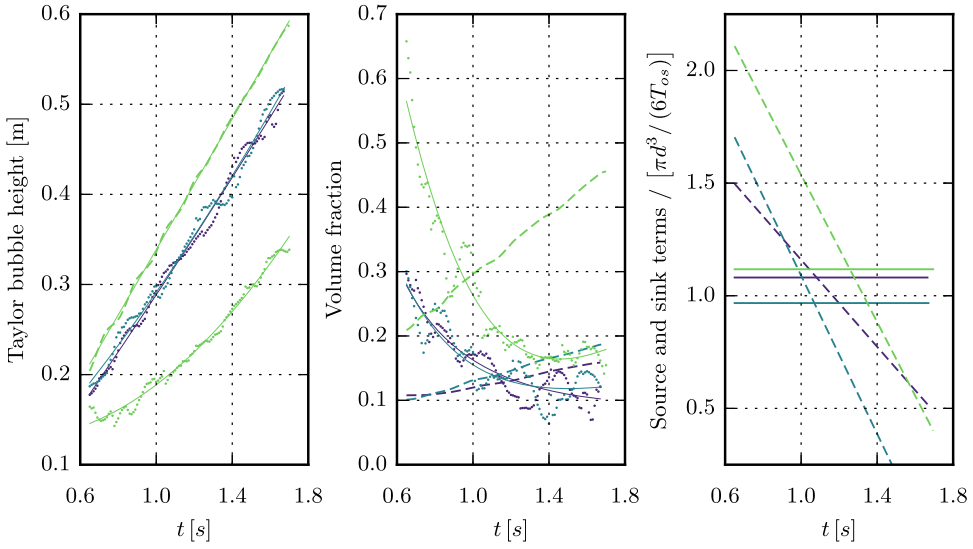

Fig. 20. Influence of the coalescence of small bubbles on the growth of the initial Taylor bubble ($t \leq T_{fb}$) for the largest three neck diameters, with from light to dark: $d^* = 0.7,\ 0.53$ and 0.44. Left: evolution of the apex position, $h_{ap}(t)$ (dashed line), and back face position, $h_{ba}(t)$ (dots) (as h_{ap} does not depend on d^*, its evolution is only reported for $d^* = 0.7$); solid line: fit used to determine the sink and source terms involved in the model. Center: evolution of the total gas volume fraction, $\langle\alpha\rangle(t)$ (dashed line), and swarm volume fraction, $\langle\alpha_{sw}\rangle(t)$ (dots); solid line: fit of experimental data. Right: fit-based estimates of the sink and source terms involved in the model, normalized by $\pi d^3/(6T_{os})$; solid line: source term $\mathcal{S}_e(t)$ due to the periodic admission of bubbles at the neck; dashed line: volumetric flow rate $\mathcal{C}_{sw\to T}(t)$ exchanged between the Taylor bubble and the trailing swarm.

ratios d^*, but smaller cylinder height-to-diameter ratios, L/D, compared to these reference experiments. The initial filling ratio, $\mathcal{F}$, was varied over a wide range. The operating conditions selected for L/D and $\mathcal{F}$ allowed us to magnify the relative duration of the initial transient stage of the discharge.

We confirmed the robustness of the flow oscillatory behavior. That is, whatever the neck diameter, the dominant response of the flow to the neck opening is periodic, even during transients involving the rise of large Taylor bubbles. Although the pressure signal becomes more complex when d^* increases, the period T_{os} remains correctly predicted by the model derived by CS. Provided $d^* \gtrsim 0.25$, the global emptying time, T_e, is also well predicted by (2) whatever the initial filling ratio, which extends the original prediction by the same authors to arbitrary values of $\mathcal{F}$.

The initial stage of the flow involves two distinct but partly (or, for large exit diameters, almost entirely) superimposed transients. The first of them, also the fastest in most cases, results from the initial expansion of the top air buffer, the volume of which has to adapt instantaneously to a new pressure condition when the gate opens. We showed that, during this first transient, the evolution of the pressure disturbance in the air buffer results from the combined effect of the hydrostatic pressure head, $\rho_l g\mathcal{F}L$ (which governs its amplitude), and the deformability of bubbles that form at the neck (which governs its decay and imposes a $d^{*3/2}$-scaling to the characteristic damping time). Thus the pressure disturbance ensures a complete coupling of the flow, from the neck to the top air buffer, and its dynamics involves gravity and capillary effects, together with two widely different spatial scales, $\mathcal{F}L$ and d. As the mass enclosed in the air buffer remains unchanged during this early stage, the upper free surface and the pressure adjust themselves, so as to ensure an approximate isothermal evolution. The second transient results from the rise of the first gas entity within the fluid column. This entity may take the form of a string of wobbling bubbles or a large Taylor bubble, depending on d^*. As this gas entity rises, the relative gas volume within the fluid column progressively increases while liquid is ejected through the neck, allowing the total volume of the column to remain almost unchanged. For $d^* \gtrsim 0.2$, the first rising gas entity exhibits a spherical cap shape, eventually turning into a large Taylor bubble, after a sufficient number of coalescence events have taken place. As soon as its front radius of curvature becomes of the order of the cylinder radius, this bubble rises with a constant speed whatever d^*. During its growth, and for large enough d^*, we could determine the gas volume fraction $\langle\alpha_{sw}\rangle$ in the bubble swarm trailed by the large bubble. We set up a simple model to explain the growth of the Taylor bubble volume, using a simple mass conservation argument giving access to the rate at which air is transferred from the swarm to the large leading bubble. The corresponding exchange volume flux, $\mathcal{C}_{sw\to T}$, is always positive and its magnitude increases with d^*, reflecting the larger number of topological changes that take place when the exit-to-cylinder diameter ratio increases.

Beyond this initial transient, a slowly-evolving discharge process takes place. The mean pressure in the top buffer increases linearly over time, while the mean liquid mass decreases with a constant rate. High-frequency oscillations induced by periodic bubble formation at the neck superimpose on these linear dynamics. Their amplitude decreases linearly over time during most of the discharge. However, during the very last stage, this amplitude tends to zero at a d^*-independent rate, presumably because the remaining oscillations result from a direct coupling between the neck and the local fluctuations of the free surface position. For a given $\mathcal{F}$, contrasting gas-liquid flows typologies were observed in the liquid region, depending on d^*. The flow structure was also found to strongly evolve over time, with marked differences between the transient stage and the subsequent slowly-evolving stage.

A natural extension of this work would consist in examining in detail the bubble formation process at the neck throughout the discharge. It would in particular shed light on the sensitivity of this process to the internal agitation of the two-phase column, which gradually increases during the discharge, owing to the chaotic motion within the bubble swarm and the sloshing of the free surface. Another aspect worthy of investigation would consist in examining the influence of the neck's length. As shown by Tehrani et al. (1992), increasing this length may change the dynamics of oscillations by adding a large pressure loss in the system. How these changes are reflected in the dynamics of bubbles released from the neck is unknown and could be investigated with the methods employed here.

We expect results obtained in the course of this investigation to be useful for further validation of multi-scale gas-liquid flow models; see Mer et al. (2018) for a discussion of issues related to predictions of some of these models in this physical configuration. Indeed, the broad variety of gas-liquid flows revealed by present observations represents a real challenge for 'large-eddy' simulation techniques. In such approaches, the two-phase flow structure is directly resolved only down to a certain scale dictated by the computational grid, while the dynamics of the subgrid-scale dispersed phase and its interactions with the resolved scales is modeled with the help of closure laws. The phenomenologies observed here for 'small' and 'large' d^* give insight into the mechanisms that need to be captured by these closure laws. For small d^*, bubbles periodically emitted at the neck undergo a few successive coalescences resulting in the creation of a swarm of bubbles with a limited size dispersion. For larger d^*, they rather undergo a large number of break-ups close to the neck, which yields the formation of bubble swarms with a high gas volume fraction and a broad size dispersion. During the initial transient stage, large spherical cap or Taylor bubbles form, thanks to the efficiency of coalescence of small bubbles 'sucked' in the wake of a larger bubble. Are current interface tracking numerical techniques combined with subgrid-scale closure models capable of dealing properly with the above 'small-to-large'-d^* transition? For instance, can advanced two-phase 'large-eddy' simulation approaches produce quantitative predictions for well-defined quantities involved in the sequence corresponding to Figs. 5 and 6, such as (*i*) the critical d^* beyond which the first rising gas entity turns into a Taylor bubble; (*ii*) the life time and maximum length reached by this bubble as a function of d^*; (*iii*) the volume-averaged gas fraction $\langle\alpha\rangle$ left in the bottle just after the Taylor bubble has burst at the free surface? These are only a few examples of simple, albeit challenging, predictions that any two-phase software aimed at predicting complex gas-liquid flows of engineering or environmental relevance should provide.

Acknowledgments

The authors acknowledge the contribution of Dandara Velasco and Cedrik Barutel who obtained and gathered the experimental data during their respective internships at IMFT.

Supplementary material

Supplementary material associated with this article can be found, in the online version, at doi:10.1016/j.ijmultiphaseflow.2019.05.012.

References

Clanet, C., Héraud, P., Searby, G., 2004. On the motion of bubbles in vertical tubes of arbitrary cross-sections: some complements to the Dumitrescu–Taylor problem. J. Fluid Mech. 519, 359–376.

Clanet, C., Searby, G., 2004. On the glug-glug of ideal bottles. J. Fluid Mech. 510, 145–168.

Davies, J.T., Taylor, G.I., 1950. The mechanics of large bubbles rising through extended liquids and through liquids in tubes. Proc. Roy. Soc. Ser. A 200, 375–390.

Deendarlianto, Höhne, T., Lucas, D., Vallée, C., Montoya Zabala, G.A., 2011. CFD studies on the phenomena around counter-current flow limitations of gas/liquid two-phase flow in a model of a PWR hot leg. Nuclear Eng. Des. 241, 5138–5148.

Dumitrescu, D.T., 1943. Stromung an einer luftblase im senkrechten rohr. Z. Angew. Math. Mech. 23, 139–149.

Fabre, J., Liné, A., 1992. Modeling of 2-phase slug flow. Annu. Rev. Fluid Mech. 24, 21–46.

Gada, V.H., Tandon, M.P., Elias, J., Vikulov, R., Lo, S., 2017. A large scale interface multi-fluid model for simulating multiphase flows. Appl. Math. Model. 44, 189–204.

Gandhi, A.B., Joshi, J.B., Kulkarni, A.A., Jayaraman, V.K., Kulkarni, B.D., 2008. SVR-based prediction of point gas hold-up for bubble column reactor through recurrence quantification analysis of LDA time-series. Int. J. Multiph. Flow 34, 1099–1107.

Hansch, S., Lucas, D., Krepper, E., Hohne, T., 2012. A multi-field two-fluid concept for transitions between different scales of interfacial structures. Int. J. Multiph. Flow 47, 171–182.

Héraud, P., 2002. Etude de la dynamique des bulles infinies: Application à l'étude de la vidange et du remplissage de réservoir. Univ. Aix-Marseille 1 Ph.D. thesis. https://tel.archives-ouvertes.fr/tel-00011664.

Jia, J., Shangguan, Z., Li, H., Wu, Y., Liu, W., Xiao, J., Kurths, J., 2016. Experimental and modeling analysis of asymmetrical on-off oscillation in coupled non-identical inverted bottle oscillators. Chaos 26, 116301.

Kohira, M.I., Kitahata, H., Magome, N., Yoshikawa, K., 2012. Plastic bottle oscillator as an on-off-type oscillator: experiments, modeling, and stability analyses of single and coupled systems. Phys. Rev. E 85, 026204.

Kordestani, S.S., Kubie, J., 1996. Outflow of liquids from single-outlet vessels. Int. J. Multiph. Flow 22, 1023–1029.

Kulkarni, A.A., Joshi, J.B., Ravi Kumar, V., Kulkarni, B.D., 2001. Application of multiresolution analysis for simultaneous measurement of gas and liquid velocities and fractional gas hold-up in bubble column using LDA. Chem. Eng. Sci. 56, 5037–5048.

Lamb, H., 1932. Hydrodynamics, 6th ed. Cambridge University Press.

Lau, Y.M., Deen, N.G., Kuipers, J.A.M., 2013. Development of an image measurement technique for size distribution in dense bubbly flows. Chem. Eng. Sci. 94, 20–29.

Mer, S., Praud, O., Neau, H., Merigoux, N., Magnaudet, J., Roig, V., 2018. The emptying of a bottle as a test case for assessing interfacial momentum exchange models for Euler-Euler simulations of multi-scale gas-liquid flows. Int. J. Multiph. Flow 106, 109–124.

Mimouni, S., Fleau, S., Vincent, S., 2017. CFD Calculations of flow pattern maps and LES of multiphase flows. Nuclear Eng. Des. 321, 118–131.

Montoya, G., Baglietto, E., Lucas, D., 2015. Implementation and validation of a surface tension model for the multi-scale approach GENTOP. In: Int. Top. Meet. Nucl. React. Therm. Hydraul. 2015, NURETH 2015, Vol. 5, pp. 4219–4232.

Raimundo, P.M., Cartellier, A., Beneventi, D., Forret, A., Augier, F., 2016. A new technique for in-situ measurements of bubble characteristics in bubble columns operated in the heterogeneous regime. Chem. Eng. Sci. 155, 504–523.

Schmidt, O., Kubie, J., 1995. An experimental investigation of outflow of liquids from single-outlet vessels. Int. J. Multiph. Flow 21, 1163–1168.

Suzanne, C., Ellingsen, K., Risso, F., Roig, V., 1998. Local measurements in turbulent bubbly flows. Nuclear Eng. Des. 184, 319–327.

Tang, S., Kubie, J., 1997. Further investigation of flow in single inlet/outlet vessels. Int. J. Multiph. Flow 23, 809–814.

Tehrani, A.A.K., Patrick, M.A., Wragg, A.A., 1992. Dynamic fluid flow behaviour of a tank draining through a vertical tube. Int. J. Multiph. Flow 18, 977–988.

Wegener, P.P., Parlange, J.Y., 1973. Spherical-cap bubbles. Annu. Rev. Fluid Mech. 5, 79–100.

Whalley, P.B., 1987. Flooding slugging and bottle emptying. Int. J. Multiph. Flow 13, 723–728.

Whalley, P.B., 1991. Two-phase flow during filling and emptying of bottles. Int. J. Multiph. Flow 17, 145–152.

Zenit, R., Rodríguez-Rodríguez, J., 2018. The fluid mechanics of bubbly drinks. Phys. Today 71, 44–50.